

# Terahertz nanoimaging and nanospectroscopy of chalcogenide phase-change materials

Chao Chen<sup>1†</sup>, Shu Chen<sup>2†</sup>, Ricardo P.S.M. Lobo<sup>3,4</sup>, Carlos Maciel-Escudero<sup>2,5</sup>, Martin Lewin<sup>6</sup>, Thomas Taubner<sup>6</sup>, Wei Xiong<sup>1</sup>, Ming Xu<sup>1\*</sup>, Xinliang Zhang<sup>1</sup>, Xiangshui Miao<sup>1</sup>, Peining Li<sup>1\*</sup>, Rainer Hillenbrand<sup>7,8\*</sup>

1. Wuhan National Laboratory for Optoelectronics & School of Optical and Electronic Information, Huazhong University of Science and Technology, Wuhan 430074, China.
2. CIC nanoGUNE BRTA, 20018 Donostia-San Sebastian, Spain.
3. LPEM, ESPCI Paris, PSL University, CNRS, 10 rue Vauquelin, 75005 Paris, France.
4. Sorbonne Université, CNRS, LPEM, 75005 Paris, France.
5. Materials Physics Center, CSIC-UPV/EHU, 20018, Donostia-San Sebastián, Spain.
6. I. Physikalisches Institut (IA), RWTH Aachen University, 52056 Aachen, Germany.
7. CIC nanoGUNE BRTA and Department of Electricity and Electronics, UPV/EHU, 20018 Donostia-San Sebastián, Spain.
8. IKERBASQUE, Basque Foundation for Science, 48013 Bilbao, Spain.

†These authors contributed equally to this work.

\*E-mail: lipn@hust.edu.cn, mxu@hust.edu.cn, r.hillenbrand@nanogune.eu

## ABSTRACT

Chalcogenide phase-change materials (PCMs) exhibit optical phonons at Terahertz (THz) frequencies, which can be used for studying basic properties of the phase transition and which lead to a strong dielectric contrast that could be exploited for THz photonics applications. Here, we demonstrate that the phonons of PCMs can be studied by frequency-tunable THz scattering-type scanning near-field optical microscopy (s-SNOM). Specifically, we perform spectroscopic THz nanoimaging of a PCM sample comprising amorphous and crystalline phases. We observe phonon signatures, yielding strong s-SNOM signals and, most important, clear spectral differences between the amorphous and crystalline PCM, which allows for distinguishing the PCM phases with high confidence on the nanoscale. We also found that the spectral signature can be enhanced, regarding both signal strength and spectral contrast, by increasing the radius of the probing tip. From a general perspective, our results establish THz s-SNOM for nanoscale structural and chemical mapping based on local phonon spectroscopy.

**KEYWORDS:** Phase-change materials, Terahertz, SNOM, nanoimaging, nanospectroscopy, optical phonons

Chalcogenide phase-change materials (PCMs) are an alloy family of germanium, antimony, and tellurium, together with some dopants. They are widely exploited in nonvolatile rewritable data storage (e.g., DVDs, Blue-ray discs, and PRAMs)<sup>1-5</sup>. PCMs normally have two stable phases at room temperature, e.g., a covalently bonded amorphous state and a crystalline state with unique “metavalent” bonds<sup>6,7</sup>, which induce large contrasts in their optical and electrical properties. Short electric or optical pulses can trigger a fast phase transition between the amorphous and crystalline states<sup>8,9</sup>. The flexible and fast switching capability makes PCMs promising for photonic applications<sup>10-13</sup>, such as high-resolution displays<sup>14</sup>, nanolenses<sup>15</sup>, optical filters<sup>16</sup>, and photonic memories<sup>17-19</sup>. Although PCMs have been mainly explored at visible and infrared frequencies<sup>20,21</sup>, they are also suitable for realizing active terahertz (THz) applications, such as THz modulators, THz optical switching and THz metamaterials<sup>22,23</sup>.

PCMs exhibit THz phonon resonances (contributing to the large THz dielectric contrast between the amorphous and crystalline states) that could enhance the performance of the THz photonic devices. Moreover, studying the THz phonon response of PCMs could also contribute to a better understanding of fundamental properties of PCMs, such as its structural transformation<sup>24</sup>, electron-phonon coupling<sup>25</sup>, and bonding mechanisms<sup>26</sup>. To date, the THz phonon response and other THz properties of PCMs have been investigated by far-field characterization methods, such as Fourier-transform spectroscopy<sup>20</sup>, differential time-domain spectroscopy<sup>27</sup>, and coherent phonon spectroscopy<sup>28</sup>. However, the spatial resolution of these methods is limited by diffraction, which does not allow for studying the local phonon response and crystallization behavior of PCMs in emerging photonic and optoelectronic nanodevices. Hence, super-resolution THz characterization methods could be highly beneficial for research and applications of PCMs.

Scattering-type scanning near-field optical microscopy (s-SNOM)<sup>29,30</sup> could enable nanoscale THz characterization<sup>31-38</sup> of PCMs. In this technique, the metallized tip of an atomic force microscope (AFM) is illuminated by *p*-polarized light. This tip acts as a broadband antenna and focuses the incident light into a nanoscale near-field spot at its sharp apex. The tip-generated near field interacts with the sample, thus transferring information of the sample into the tip-scattered field, which can be detected by a far-field detector. By scanning the tip across the sample, near-field images with nanoscale spatial resolution can be recorded. The spatial resolution of s-SNOM is determined essentially by the tip apex radius (typically around 20 nm) rather than by the wavelength of the light. Recently, s-SNOM has been applied for characterizing PMCs at mid-infrared frequencies<sup>39-41</sup>, however, THz s-SNOM studies of PCMs and particularly of their phonon resonances has been elusive so far.

Here, we report the first THz near-field study of a prototype chalcogenide PCMs, Ge<sub>1</sub>Te<sub>2</sub>Sb<sub>4</sub> compounds (in short GST), employing a state-of-the-art s-SNOM combined with a tunable THz gas laser. We recorded near-field spectroscopic data of a GST sample comprising both amorphous (a-) and crystalline (c-) states. Corroborated by theoretical calculations, we demonstrate that the measured near-field spectra reveal distinct phonon signatures of the a-GST and c-GST states. We further demonstrate that the phonon-induced spectral signatures can be

enhanced, regarding both signal strength and spectral contrast, by increasing the radius of the probing tip. Our results thus establish THz s-SNOM for the nanoidentification of distinct PCM states based on local phonon spectroscopy.

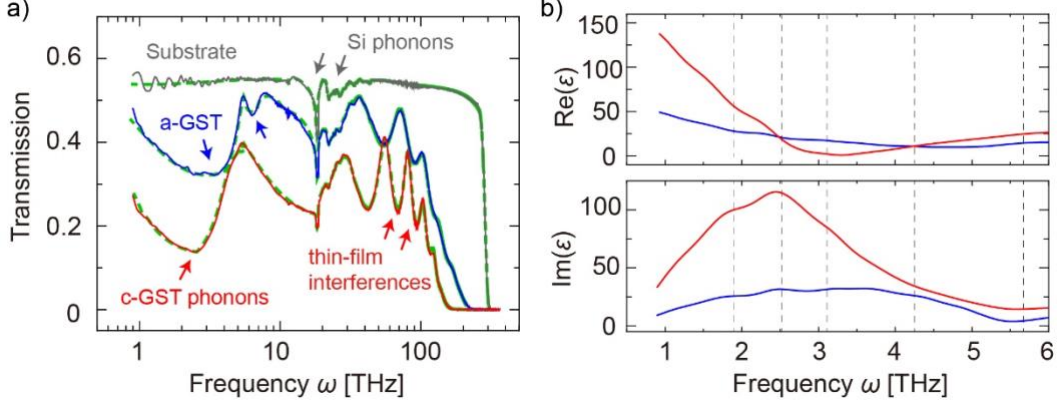


**Fig. 1 Far-field THz properties of GST.** (a) FTIR transmission spectra of GST films: a-GST (blue curve), c-GST (red curve) and bare silicon substrate (gray curve). The dashed green curves are the fitted results for extracting the dielectric functions. (b) Dielectric functions of a-GST (blue curve) and c-GST (red curve), extracted from the measured transmission spectra. The real part  $\text{Re}(\epsilon)$  and imaginary part  $\text{Im}(\epsilon)$  are shown in the top panel and bottom panel, respectively. Vertical dashed lines mark the available operation frequencies of the THz gas laser used in the near-field measurements.

We first measured far-field optical properties of GST films (sample details in the methods) by using an ultra-broadband Fourier transform spectrometer (spanning from 0.9 THz to 350 THz). Fig. 1a shows the transmission spectra of a-GST (blue curve), c-GST (red curve) and bare silicon substrate (gray curve). The transmittance of the undoped silicon substrate is nearly constant in the measured region, except for the dips at around 18.5 THz (marked with gray arrows), which are caused by a second order phonon absorption<sup>42</sup>. Both spectra of a-GST and c-GST thin films display several peaks at high frequencies ( $>30$  THz) due to the thin-film interferences. For lower frequencies (1-10 THz), the spectrum of the a-GST exhibits two dips (indicated by blue arrows) at the spectrum positions of the phonon modes reported for the a-GST<sup>20</sup>. In contrast, the c-GST state possessing a higher refraction-index exhibits a lower transmission over the whole spectral range, accompanying with only a broad phonon absorption dip at around 2.5 THz. The red-shift of the broad absorption dip (from a-GST to c-GST) can be explained by the phonon softening upon crystallization<sup>43</sup>. The dielectric functions of the two GST states shown in Fig.1b are extracted from transmission spectrum by using a thin-film matrix model, in which the GST layer and the substrate are described by an Abeles matrix<sup>44-46</sup> (see the fitted transmission spectra perfectly matching the experimental data: the dashed green curves in Fig. 1a). The imaginary parts of dielectric functions show that c-GST has larger absorption than a-GST owing to a stronger phonon mode. We emphasize that the obtained dielectric functions of a- and c-GST states do not only provide a reference for evaluating and understanding subsequent near-field measurements, they are also important databases that can

be used for the design and optimization of GST-based THz nanophotonic optoelectronic elements and devices.

For THz near-field measurements, we used a commercial s-SNOM setup (Neaspec GmbH, sketch in Fig. 2a) based on a tapping-mode AFM. The laser beam of a wavelength-tunable THz gas laser (SIFIR-50, Coherent Inc., USA) is focused on the sharp metallic AFM tip by a parabolic mirror<sup>31</sup>. The back-scattered light from the tip is collected by a cryogen-free THz Bolometer System (QMC Instruments Ltd. 2019). To suppress the contributions of background signals, the tip is vibrated at the cantilever's mechanical oscillation frequency  $\Omega \approx 270$  kHz with an amplitude of 200 nm and the detector signal is demodulated at higher harmonics  $n\Omega$  ( $n \geq 2$ ). Near-field amplitude and phase signals,  $s_n$  and  $\varphi_n$ , were mapped via synthetic optical holography (SOH)<sup>47</sup>, which is based on a Michelson interferometer where the reference mirror (mounted on a delay stage) is translated with constant velocity along the reference beam path<sup>48,49</sup>. The investigated sample system is shown in the inset of Fig. 2b. A 130-nm-thick as-deposited a-GST film was prepared on a SiO<sub>2</sub>/Si substrate and a femtosecond laser was used to optically switch several areas (marked by red, size:  $15 \times 15 \mu\text{m}^2$ , deeply subwavelength for the THz regime) to the crystalline state (details in Methods).

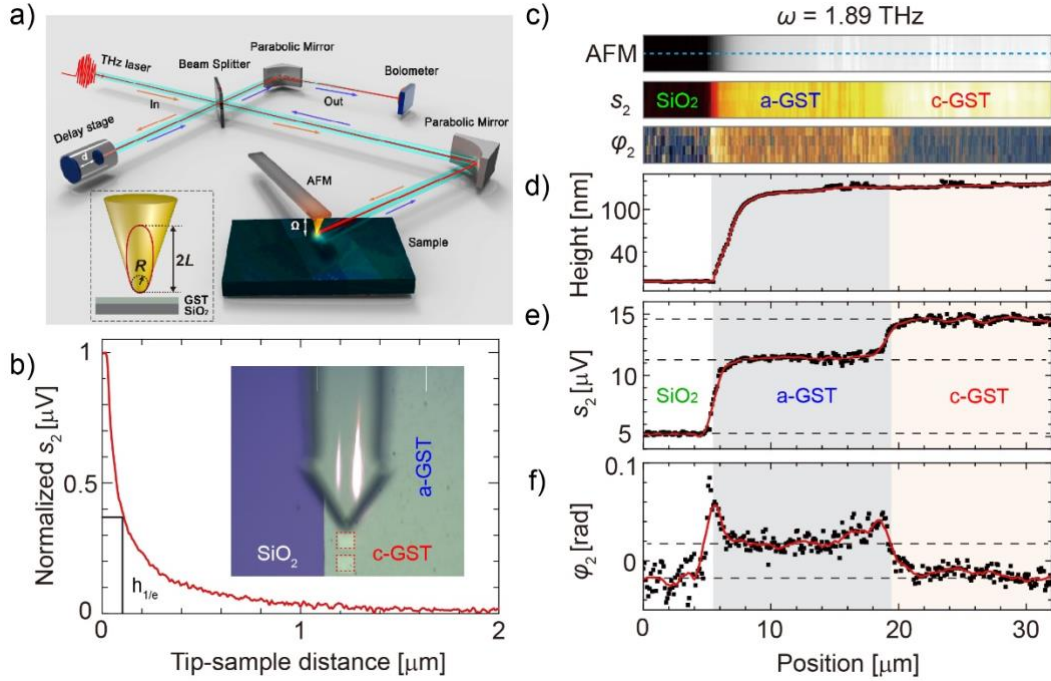


**Fig. 2 THz near-field setup and imaging experiments.** (a) Schematics of the THz s-SNOM setup with a bolometer as a detector. The inset shows an illustration of the finite dipole model for the layered sample. (b) Approach curve, showing the amplitude signal  $s_2$  on c-GST as a function of tip-sample distance. The mark  $h_{1/e}$  represents the position at which the signal decays to  $1/e$  of its maximum. The inset displays an optical microscope image of the AFM tip above the sample. The red dotted squares mark the c-GST areas. (c) AFM topography image (top panel) of GST on a silicon oxide substrate, which includes amorphous and crystalline state. Near-field amplitude ( $s_2$ , middle panel) and phase ( $\varphi_2$ , bottom panel) images at 1.89 THz. (d) Topography, (e) near-field amplitude, and (f) phase line profiles (shown as solid symbols) taken

from the corresponding images in c. The red solid lines are smoothed curves based on the experimental data. Horizontal dashed gray lines are a guide for the eye.

To characterize our THz s-SNOM set-up, we first measured near-field amplitude approach curves. To that end, we recorded amplitude signal  $s_n$  as a function of the tip-sample distance. We used a commercial Pt/Ir tip (model ARROW-NCPT, Nanoworld) of radius  $R = 25$  nm and tip length of about  $20 \mu\text{m}$ .<sup>49</sup> Fig. 2b presents the amplitude signal  $s_2$  as a function of tip-sample distance, which was measured on the c-GST area at a frequency of 1.89 THz (note that the curve is normalized to its maximum value at contact). The measured  $s_2$  signal exhibits a decay distance of about 110 nm (obtained at the height at the  $1/e$  of the maximum) and further decreases to almost zero at large distances, indicating an efficient suppression of the background signal. We thus recorded the  $s_2$  signal in all near-field imaging experiments shown in this work.

To record near-field images, we performed line scans across the substrate, the a-GST and c-GST areas. The obtained results are shown together with the simultaneously measured AFM topography in Fig. 2c. From the AFM topography (line profile in Fig. 2d), the a-GST and c-GST areas are difficult to distinguish as the phase transition only causes a small volume change ( $< 7\%$ ). In contrast, they can be identified in the near-field amplitude  $s_2$  and phase  $\varphi_2$  images due to their distinct THz properties. The c-GST area exhibits larger  $s_2$  signals and smaller  $\varphi_2$  signals as compared with the a-GST area (line profiles in Fig. 2e and f). These two images thus verify the capability of the s-SNOM for near-field identification of different GST states in the THz spectral range.

To reveal near-field spectroscopic properties of the GST, we repeated the near-field line scans at five different frequencies with the standard tip of apex radius  $R = 25$  nm. The measured data set (Fig. 3a and b) shows that near-field signals of the GST states vary upon frequency change. For quantification of the frequency dependence, we extracted normalized amplitude and phase signals (defined as  $s_2^{\text{GST}}/s_2^{\text{SiO}_2}$  and  $\varphi_2^{\text{GST}} - \varphi_2^{\text{SiO}_2}$ ) and plotted them in Fig. 3c-f. We observe that the amplitude and phase signals of both GST phases display strong but different spectral variations, demonstrating that the two distinct phonon resonances of a- and c-GST can be locally probed and distinguished by spectroscopic THz s-SNOM. We note that in the near-field phase images taken at 2.52 THz the a-GST edge and interface to c-GST appear brighter than the interior of the a-GST area, which might indicate a slightly modified dielectric response (eventually caused by local strain, or other physical or chemical effects), at the boundaries of the a-GST area. Future studies will be needed for clarifying this interesting observation.

To corroborate and analyze in more detail the near-field spectroscopic contrasts between the two different GST states, we performed theoretical calculations based on the Finite Dipole Model (FDM)<sup>50</sup> of s-SNOM for layered samples<sup>51</sup>. The metallic AFM tip is modeled as an elongated conducting spheroid with major-axis length  $2L$  and apex radius  $R$  (sketch in the inset of Fig. 2a,  $R = 25$  nm,  $L = 10R$  according to ref. 50). The sample is described by the momentum-dependent ( $q$ -dependent) Fresnel reflection coefficient  $r_p(q)$  of the 130 nm thick GST film on the (semi-infinite)  $\text{SiO}_2$  substrate. Within the FDM model we use the Fresnel reflection coefficient at  $q = 1000k_0$  (normalized to the momentum of free-space photons  $k_0$ ), considering

that the near fields at the nanoscale tip apex are deep subwavelength scale (with a large momentum dominated at  $q = 1/R \sim 1000k_0$ , for  $R = 25$  nm and the free space wavelength  $\lambda = 100$   $\mu\text{m}$ ). The calculated the s-SNOM amplitude  $s_2$  and phase  $\varphi_2$  spectra (normalized to the SiO<sub>2</sub> substrate) for the a- and c-GST film are shown in Fig. 3c-f. They match well the experimental data, particularly reproducing the peaks observed in near-field phase spectra. Discrepancies between the experimental and calculated values may stem from the THz antenna response of the metallic tip and the adjacent cantilever<sup>52</sup>, which are not considered in the FDM. The vibrational resonance of both phases can be identified by its typical near-field spectroscopy signature<sup>53</sup>: a rather large  $s_2$ -signal (dashed lines in Fig. 3c and e) is followed by a clear minimum at higher frequencies (4.8 THz for c-GST and 5.2 THz for a-GST), and accompanied by a maximum in the  $\varphi_2$ -spectrum that is located between the  $s_2$ -maximum and  $s_2$ -minimum (dashed lines in Fig. 3d and f).

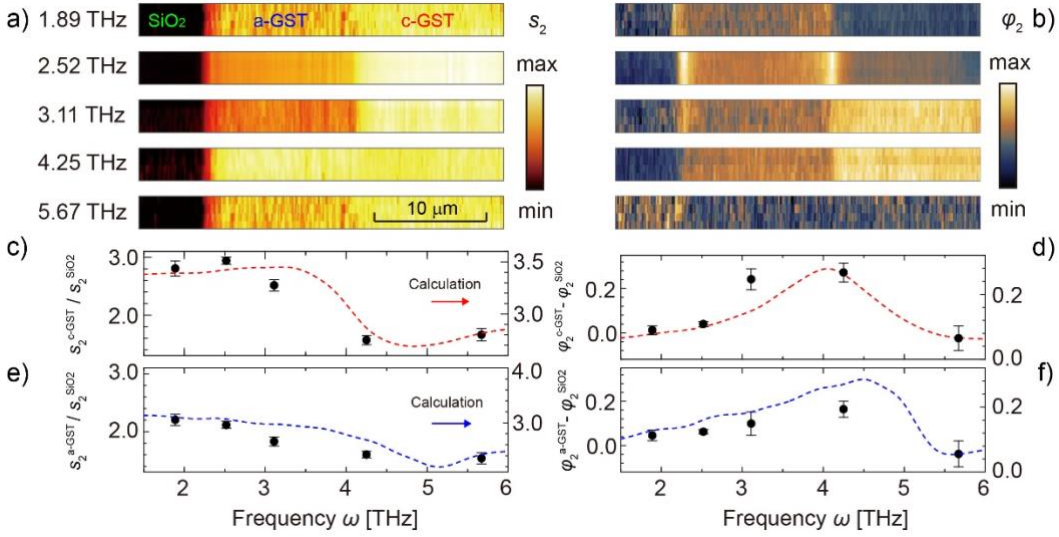


**Fig. 3 THz spectroscopic near-field measurements.** (a) Near-field amplitude  $s_2$  images and (b) phase  $\varphi_2$  images obtained by scanning across the substrate/a-GST/c-GST areas, taken at five different frequencies. (c-f) Symbols: measured near-field spectra, taken from the images shown in (a) and (b). Dashed curves: calculated near-field spectra by using the dielectric functions of c-GST (dashed red lines) and a-GST (dashed blue lines) shown in Fig. 1.

It has been recently shown that the strength of s-SNOM signals can be enhanced by increasing the tip apex radius<sup>49</sup>, which is of critical importance for s-SNOM particularly at THz frequencies, as the power of currently available THz sources is often much lower than that of sources in the infrared or visible spectral range. In the following, we thus investigate how near-field signals of c- and a-GST depend on the apex radius of s-SNOM tips. To this end, we repeated the line scans shown in Fig. 3 using tips with larger apex radius ( $R = 250$  nm and 500 nm)(model LRCH, Team Nanotec). Tapping amplitude  $A = 200$  nm, demodulation order and laser power for a specific frequency were kept the same. However, changing both the frequency and the tip requires repeated readjustment of the setup (focusing mirror and interferometer). Although it was done such that the maximum near-field amplitude signal  $s_2$  was obtained for each measurement, we cannot exclude measurement uncertainties. For that reason, the

measurements shown and discussed in Fig. 4 have to be considered as qualitative study for estimating the signal enhancement.

Fig. 4a and b show near-field amplitude  $s_2$  profiles that were recorded with three different tips at two different laser frequencies. For each frequency, the different tips yield similar line profiles. However, and most importantly, the amplitude signal  $s_2$  is strongly enhanced for all three areas (SiO<sub>2</sub>, a- and c-GST) when the tip apex radius  $R$  is increased. On the other hand, the line profiles obtained with larger tips exhibit a larger signal dip at the edge between the a-GST film and the SiO<sub>2</sub> substrate, indicating a more pronounced edge darkening artefact<sup>54</sup>. Further, the signal transition between the two GST states is extended because of the reduced spatial resolution. Still, we can estimate a deep subwavelength-scale spatial resolution better than 1  $\mu\text{m}$  ( $< \text{THz wavelength}/100$ ). We also see more (noise-like) signal fluctuations, which we attribute to less stable AFM operation and surface roughness, the later leading to more pronounced artefacts (similar to edge darkening artefact) when the tip radius increases.

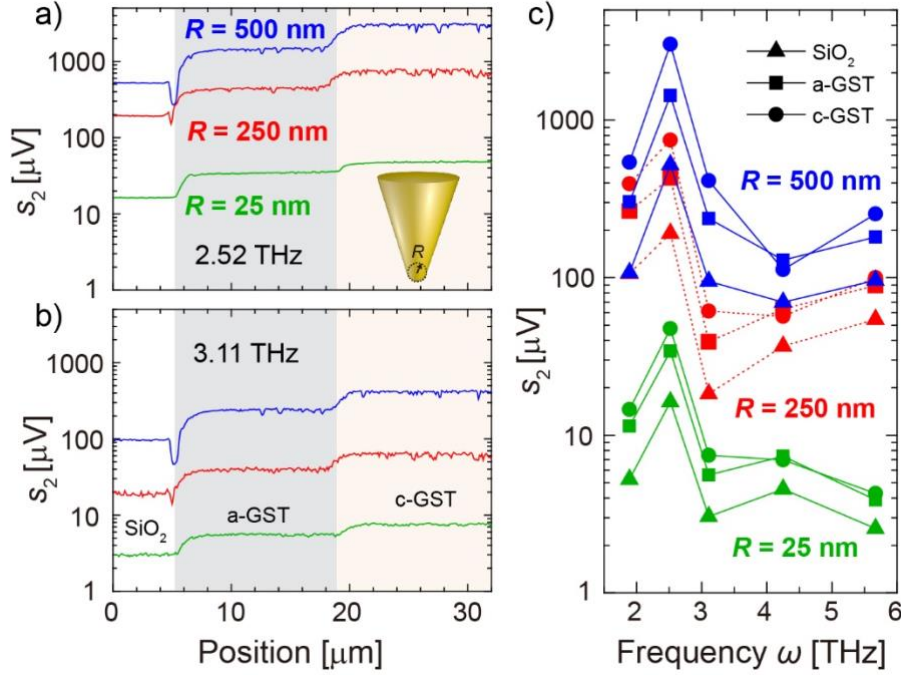


**Fig. 4 Near-field signal enhancement by increasing the tip apex radius.** (a,b) Near-field amplitude ( $s_2$ ) line profiles recorded at 2.52 and 3.11 THz using tips with apex radius  $R = 25 \text{ nm}$ , 250 nm and 500 nm. (c) Averaged  $s_2$  signals on c-GST (solid circle), a-GST (solid square) and SiO<sub>2</sub> (solid triangle) as a function of frequency, obtained with tips  $R = 500 \text{ nm}$  (blue symbols), 250 nm (red symbols) and  $R = 25 \text{ nm}$  (green symbols).

For more detailed evaluation of the signal enhancement provided by the larger tips, we show in Fig. 4c the averaged values of the  $s_2$  signals on c-GST (solid circles), a-GST (solid squares) and SiO<sub>2</sub> (solid triangles) as a function of frequency for the three tips. We can clearly see that the amplitude signal  $s_2$  can be enhanced by one to two orders of magnitude when using a tip with apex radius  $R = 500 \text{ nm}$  (blue symbols) instead of a standard tip with apex radius  $R = 25 \text{ nm}$  (green symbols). Note that the spectral behavior observed in Fig. 4c depends on both the

spectroscopic features of the sample and the frequency-dependent laser power, as the near-field amplitude signals were not normalized to a reference sample as typically done in s-SNOM (after such normalization the information about the enhancement of absolute near-field signals is lost).

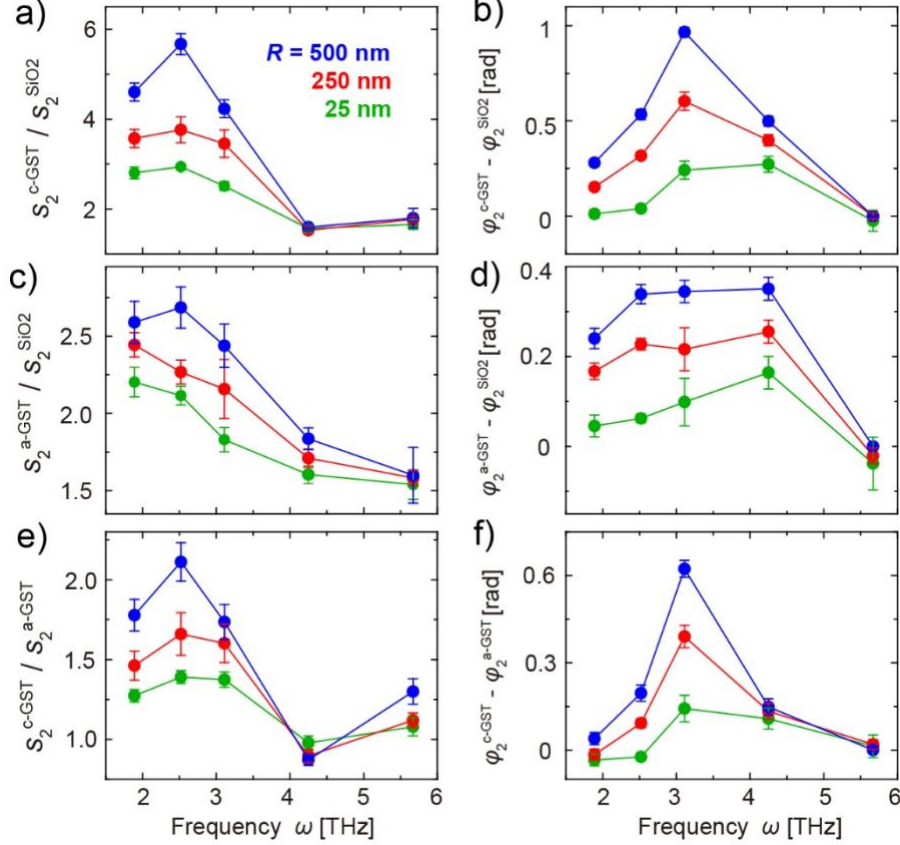


**Fig. 5 Tip-size dependence of the near-field spectroscopic contrasts.** Near-field (a) amplitude  $s_2$  and (b) phase  $\varphi_2$  contrasts between a-GST and  $\text{SiO}_2$  for different tip radii:  $R = 500$  nm (blue symbols),  $R = 250$  nm (red symbols) and  $R = 25$  nm (green symbols). Near-field (c) amplitude  $s_2$  and (d) phase  $\varphi_2$  contrasts between c-GST and  $\text{SiO}_2$  for different tip radii. Near-field (e) amplitude  $s_2$  and (f) phase  $\varphi_2$  contrasts between c-GST and a-GST for different tip radii.

Having demonstrated the significant enhancement of the absolute near-field amplitude signals, we aim in the following to study the typical spectroscopic s-SNOM contrasts, that is, when the near-field amplitude and phase signals of a sample (here GST) are normalized to a spectroscopically flat reference sample (here  $\text{SiO}_2$ ) in order to eliminate spectral features that are caused by frequency-dependent laser power and setup alignment uncertainties. Fig. 5a-d show the near-field amplitude and phase contrasts of c- and a-GST (defined as  $s_2^{\text{c-GST}}/s_2^{\text{SiO}_2}$  and  $\varphi_2^{\text{c-GST}} - \varphi_2^{\text{SiO}_2}$ , respectively  $s_2^{\text{a-GST}}/s_2^{\text{SiO}_2}$  and  $\varphi_2^{\text{a-GST}} - \varphi_2^{\text{SiO}_2}$ ). It is seen that the variation of the tip apex radius modifies both the near-field amplitude and phase contrasts, and that this modification strongly depends on the frequency. Specifically, the near-field contrasts of the c-GST (Fig.5a and b) are enhanced by the large tips at frequencies close to the optical phonon mode (at around 2.5 THz, indicated by the peak of  $\text{Im}(\epsilon)$  shown in Fig.1b), where we observe

a peak in the amplitude-contrast peak at 2.52 THz and a peak in the phase contrast at 3.11 THz, respectively. Away from the phonon frequency at 5.67 THz, in contrast, all three different tips yield a similar contrasts. The observations for the a-GST shown in Fig.5c and d are similar to that of c-GST. **We explain the contrast enhancement by the reduction of the relative tapping amplitude when the apex radius is increased while the absolute tapping amplitude is kept constant.** Enhanced material contrast in s-SNOM is a well-known phenomenon, which occurs when the harmonic demodulation order  $n$  is increased, or when the tapping amplitude relative to the tip radius is reduced<sup>48,49,55-58</sup>. The contrast enhancement typically depends on the sample permittivity, and thus on the frequency in case of a frequency-dependent permittivity<sup>58</sup> as is the case for GST around its phonon frequency (Fig. 1b).

The enhancement of the contrast of each of the GST states relative to the SiO<sub>2</sub> substrate also leads to enhanced amplitude and phase contrasts between c- and a-GST (defined as  $s_2^{\text{c-GST}}/s_2^{\text{a-GST}}$  and  $\varphi_2^{\text{c-GST}} - \varphi_2^{\text{a-GST}}$ , respectively) when tips with larger apex radius are used (Fig. 5e,f). The contrast enhancement is strongest at frequencies close to the phonon mode, allowing for the most efficient distinguishing of GST states at these frequencies.

For a better qualitative understanding of the strong spectral variation of the contrast enhancement with increasing tip apex radius, we performed calculations using the point dipole model<sup>59</sup>, as it can be readily applied to THz frequencies, layered samples and large tip radii (which is less straight forward with more sophisticated s-SNOM models). The tip is modelled by a metallic sphere of a radius that corresponds to the tip apex radius  $R$ , oscillating vertically with tapping amplitude  $A$ . Figure 6a-c shows the calculated demodulated amplitude and phase spectra of a 130 nm thick c-GST layer on SiO<sub>2</sub> for sphere radii of  $R = 25$  nm (green curves) and 250 nm (red curves) for different tapping amplitudes. All of them show the same qualitative spectral behavior as observed in the experiment (Figs. 3 and 5) and with the finite dipole model (Fig. 3), demonstrating the suitability of the model for a qualitative description of the experimental THz s-SNOM data. Most importantly, the model confirms the enhanced spectral contrast for the larger tip radius, that is, that the amplitude and phase contrast enhancement factors,  $f_s = [s_2^{\text{c-GST}}(R = 250 \text{ nm})/s_2^{\text{SiO}_2}(R = 250 \text{ nm})] / [s_2^{\text{c-GST}}(R = 25 \text{ nm})/s_2^{\text{SiO}_2}(R = 25 \text{ nm})]$  and analogously  $f_\varphi$ , depend on the permittivity  $\varepsilon(\omega)$  and thus on  $\omega$ . We also notice a strong dependency of the contrast enhancement on the tapping amplitude  $A$  (Fig. 6d). Interestingly, for  $A = 160$  nm we find a clear contrast enhancement below 4 THz for the larger tip ( $f_s > 1$ ), which, however, vanishes around 4.5 THz ( $f_s \approx 1$ ), similarly to our experimental observations. A further increase of  $A$  even yields a reduction of the amplitude contrast at 4.5 THz. We explain this finding by the finite thickness of the c-GST sample and the increased near-field probing depth<sup>60</sup> at larger tapping amplitudes and for larger tip radii. For these reasons, more of the SiO<sub>2</sub> substrate (i.e. less c-GST relative to the total probing volume) is probed when the c-GST layer becomes more transparent for the tip's near fields around 4.5 THz. We stress that the experimentally observed vanishing s-SNOM amplitude contrast enhancement with tip radius at a specific frequency is not an intrinsic sample property, but strongly depends on material properties (permittivity, layer thickness) and s-SNOM parameters (tapping amplitude, tip radius, demodulation order). We envision a more quantitative description of tip-size-dependent near-field contrasts with the help of more sophisticated s-SNOM modelling in the future.

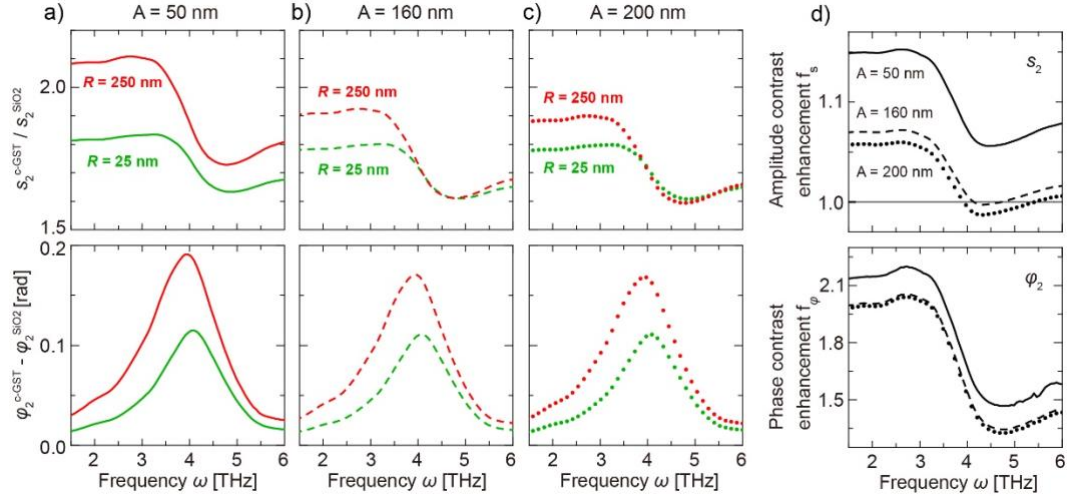


**Fig. 6 Dipole model calculation of near-field contrasts for a 130 nm thick c-GST layer on SiO<sub>2</sub>.** (a-c) Amplitude and phase contrast as function for different tip radii  $R$  and tapping amplitudes  $A$ . (d) Amplitude and phase contrast enhancement  $f_s$  and  $f_\phi$  for different tapping amplitudes.

In summary, we performed the first THz near-field imaging and spectroscopy of a chalcogenide PCM sample – a GST film comprising both a- and c-GST states. The obtained near-field spectra reveal clear spectral differences between a- and c-GST, which allows for distinguishing the GST state with high confidence and nanoscale resolution. We further show that both the near-field THz signal strengths and the spectroscopic contrasts of the GST states can be enhanced by increasing the s-SNOM tip radius. Importantly, this enhancement is strongly frequency dependent. It is more pronounced near the phonon resonances as compared to frequencies far away from the phonon. These results establish THz s-SNOM for structural and chemical nanospectroscopy based on local phonon spectroscopy. Our work also opens a new avenue for characterizing the PCMs in the THz region with nanoscale spatial resolution and the results could be instructive for further s-SNOM characterization of PCMs-based THz photonic and electronic devices for practical semiconductor industry applications. We envision that by implementing ultrafast pump-probe THz s-SNOM<sup>30,61,62</sup> even the transient structural phase transformation in GST could be studied by nanoscale phonon spectroscopy.

## **METHODS**

For transmission measurements the GST sample in Fig. 1 was deposited by DC magnetron sputtering onto highly resistive ( $> 5000 \text{ k}\Omega\cdot\text{cm}$ ) silicon (100) wafers (double-sided polished). A direct current power of 30 W was applied to the corresponding target in an atmosphere of 0.5 Pa argon. GST films (about 930 nm thickness) were deposited as amorphous state and then annealed in an oven at 155 °C for half an hour to be face-centered cubic (fcc) phase determined by XRD spectra.

For s-SNOM measurements the GST (about 130 nm thickness) sample were deposited by DC magnetron sputtering onto silicon (100) substrates covered with 1  $\mu\text{m}$  SiO<sub>2</sub>. The laser switching process of the GST sample was conducted in an in-house-built set-up by focusing a laser beam through a 40 objective on the sample surface. A femtosecond laser with a central wavelength of 800 nm provides pulses with tunable output power (up to 1400 mW), pulse duration of 100 fs and repetition frequency of 80 MHz. To realize a crystallization process, we used pulses with a power of 10 mW and a spot diameter of 4  $\mu\text{m}$ . An x-y movable sample stage moved at the speed of 30  $\mu\text{m}/\text{s}$  with a minimal step size of 1  $\mu\text{m}$  was used to prepare the structures shown in Fig. 2. The crystallized areas are fcc phase determined by Raman spectra.

## **ACKNOWLEDGEMENT**

The authors are grateful to Prof. Matthias Wuttig from RWTH Aachen and Dr. Stefan Mastel from Neaspec GmbH for useful discussions. C.C. acknowledges the Postdoctoral Fund of Hubei Province (Grant No. 182/0106182067). M.X. acknowledges the National Key R&D Plan of China (Grant No. 2017YFB0701701 “Materials Genome Engineering”) and the National Natural Science Foundation of China (Grant No. 51772113). M.L. and T.T. acknowledge funding from the DFG (German Science Foundation) within the collaborative research center SFB 917 “Nanoswitches”. P. L. acknowledges the National Natural Science Foundation of China (Grant No. 62075070). R.H. acknowledges financial support from the European Union's H2020 FET OPEN project PETER (GA#767227), the Spanish Ministry of Science, Innovation and Universities (national project RTI2018-094830-B-100 and the project MDM-2016-0618 of the Marie de Maeztu Units of Excellence Program) and the Basque Government (grant No. IT1164-19).

## **COMPETING FINANCIAL INTERESTS**

R.H. is cofounder of Neaspec GmbH, a company producing scattering type scanning near-field optical microscope systems, such as the one used in this study. The remaining authors declare no competing financial interests.

## REFERENCES

- (1) Wuttig, M.; Yamada, N. Phase-change materials for rewriteable data storage. *Nat. Mater.* **2007**, *6*, 824–832.
- (2) Ding, K.; Wang, J.; Zhou, Y.; Tian, H.; Lu, L.; Mazzarello, R.; Jia, C.; Zhang, W.; Rao, F.; Ma, E. Phase-change heterostructure enables ultralow noise and drift for memory operation. *Science* **2019**, *366*, 210–215.
- (3) Zhang, W.; Mazzarello, R.; Wuttig, M.; Ma, E. Designing crystallization in phase-change materials for universal memory and neuro-inspired computing. *Nat. Rev. Mater.* **2019**, *4* (3), 150–168.
- (4) Tuma T., Pantazi, A.; Le Gallo, M.; Sebastian, A.; Eleftheriou, E. Stochastic phase-change neurons. *Nat. Nanotechnol.* **2016**, *11*, 693.
- (5) Salinga, M.; Kersting, B.; Ronneberger, I.; Jonnalagadda, V. P.; Vu, X. T.; Le Gallo, M.; Giannopoulos, I.; Cojocaru-Mirédin, O.; Mazzarello, R.; Sebastian, A. Monatomic phase change memory. *Nat. Mater.* **2018**, *17* (8), 681–685.
- (6) Kooi, B. J.; Wuttig, M. Chalcogenides by Design: Functionality through Metavalent Bonding and Confinement. *Adv. Mater.* **2020**, *32* (21), 1908302.
- (7) Zhu, M.; Cojocaru-Mirédin, O.; Mio, A. M.; Keutgen, J.; Küpers, M.; Yu, Y.; Cho, J. Y.; Dronskowski, R.; Wuttig, M. Unique bond breaking in crystalline phase change materials and the quest for metavalent bonding. *Adv. Mater.* **2018**, *30* (18), 1706735.
- (8) Pirovano, A.; Lacaita, A. L.; Benvenuti, A.; Pellizzer, F.; Bez, R. Electronic switching in phase-change memories. *IEEE Trans. Electron Devices* **2004**, *51*, 452–459.
- (9) Kolobov, A. V.; Fons, P.; Frenkel, A. I.; Ankudinov, A. L.; Tominaga, J.; Uruga, T. Understanding the phase-change mechanism of rewritable optical media. *Nat. Mater.* **2004**, *3* (10), 703–708.
- (10) Ikuma, Y.; Saiki, T.; Tsuda, H. Proposal of a small self-holding 2×2 optical switch using phase-change material. *IEICE Electron. Express* **2008**, *5*, 442–445.
- (11) Wuttig, M.; Bhaskaran, H.; Taubner, T. Phase-change materials for non-volatile photonic applications. *Nat. Photonics* **2017**, *11*, 465–476.
- (12) Chaudhary, K.; Tamagnone, M.; Yin, X.; Capasso, F. Polariton nanophotonics using phase-change materials. *Nat. Commun.* **2019**, *10* (1), 4487.
- (13) Cao, T.; Cen, M. J. Fundamentals and Applications of Chalcogenide Phase-Change Material Photonics. *Adv. Theory Simul.* **2019**, *2* (8), 1900094.
- (14) Rios, C.; Hosseini, P.; Taylor, R. A.; Bhaskaran, H. Color Depth Modulation and Resolution in Phase-Change Material Nanodisplays. *Adv. Mater.* **2016**, *28*, 4720–4726.
- (15) Wang, Q.; Rogers, E. T. F.; Gholipour, B.; Wang, C.; Yuan, G.; Teng, J.; Zheludev, N. I. Optically reconfigurable metasurfaces and photonic devices based on phase change materials. *Nat. Photonics* **2016**, *10*, 60–66.

- (16) Rudé, M. J.; Zalden, P.; Chen, F.; Weems, B.; Chatzakis, I.; Xiong, F.; Jeyasingh, R.; Hoffmann, M. C.; Pop, E.; Wong, H. S. P.; Wuttig, M.; Lindenberg, A. M. Ultrafast and Broadband Tuning of Resonant Optical Nanostructures Using Phase-Change Materials. *Adv. Opt. Mater.* **2016**, *4*, 1060–1066.
- (17) Cao, T.; Liu, K.; Lu, L.; Liu, J. X.; Liu, Y. J.; Qin, K. R.; Chui, H. C.; Simpson, R. E. All-Photonic Phase-Change Memories: Low-Power Phase Transition of Chalcogenide Glass Using Au Nanoparticle Plasmon Resonance. *Adv. Opt. Mater.* **2020**, *8* (6), 2070025.
- (18) Ríos, C.; Stegmaier, M.; Hosseini, P.; Wang, D.; Scherer, T.; Wright, C. D.; Bhaskaran, H.; Pernice, W. H. P. Integrated all-photonic non-volatile multi-level memory. *Nat. Photonics* **2015**, *9*, 725–733.
- (19) Pernice, W. H. P.; Bhaskaran, H. Photonic non-volatile memories using phase change materials. *Appl. Phys. Lett.* **2012**, *101*, 171101.
- (20) Bragaglia, V.; Holldack, K.; Boschker, J. E.; Arciprete, F.; Zallo, E.; Flissikowski, T.; Calarco, R. Far-Infrared and Raman Spectroscopy Investigation of Phonon Modes in Amorphous and Crystalline Epitaxial GeTe-Sb<sub>2</sub>Te<sub>3</sub> Alloys. *Sci. Rep.* **2016**, *6*, 28560.
- (21) Shportko, K.; Zalden, P.; Lindenberg, A. M.; Rückamp, R.; Grüninger, M. Anharmonicity of the vibrational modes of phase-change materials: A far-infrared, terahertz, and Raman study. *Vib. Spectrosc.* **2018**, *95*, 51–56.
- (22) Miller, K. J.; JR. Haglund, R. F.; Weiss, S. M. Silicon waveguide optical switch with embedded phase change material. *Opt. Mater. Express* **2018**, *8* (8), 2415.
- (23) Pitchappa, P.; Kumar, A.; Prakash, S.; Jani, H.; Venkatesan, T.; Singh, R. Chalcogenide Phase Change Material for Active Terahertz Photonics. *Adv. Mater.* **2019**, *31* (12), 1808157.
- (24) Steigmeier, E. F.; Harbeke, G. Soft phonon mode and ferroelectricity in GeTe. *Solid State Commun.* **1970**, *8* (16), 1275–1279.
- (25) Ruckhofer, A.; Campi, D.; Bremholm, M.; Hofmann, P.; Benedek, G.; Bernasconi, M.; Ernst, W. E.; Tamtögl, A. Terahertz Surface Modes and Electron-Phonon Coupling in Bi<sub>2</sub>Se<sub>3</sub>(111). *Phys. Rev. Research* **2020**, *2* (2), 023186.
- (26) Mukhopadhyay, S.; Sun, J.; Subedi, A.; Siegrist, T.; Singh, D. J. Competing covalent and ionic bonding in Ge-Sb-Te phase change materials. *Sci. Rep.* **2016**, *6*, 25981.
- (27) Makino, K.; Kato, K.; Saito, Y.; Fons, P.; Kolobov, A. V.; Nakajima, M. Terahertz spectroscopic characterization of Ge<sub>2</sub>Sb<sub>2</sub>Te<sub>5</sub> phase change materials for photonics applications. *J. Mater. Chem. C* **2019**, *7* (27), 8209–8215.
- (28) Hase, M.; Fons, P.; Mitrofanov, K.; Kolobov, A. V.; Tominaga, J. Femtosecond structural transformation of phase-change materials far from equilibrium monitored by coherent phonons. *Nat. Commun.* **2015**, *6* (1), 8367.
- (29) Keilmann, F.; Hillenbrand, R. Near-field microscopy by elastic light scattering from a tip. *Phi. Trans. R. Soc. Lond. A* **2004**, *362*, 787–805.
- (30) Chen, X.; Hu, D.; Mescall, R.; You, G.; Basov, D. N.; Dai, Q.; Liu, M. Modern Scattering-Type Scanning Near-Field Optical Microscopy for Advanced Material Research. *Adv. Mater.*

**2019**, *31* (24), 1804774.

(31) Huber, A. J.; Keilmann, F.; Wittborn, J.; Aizpurua, J.; Hillenbrand, R. Terahertz Near-Field Nanoscopy of Mobile Carriers in Single Semiconductor Nanodevices. *Nano Lett.* **2008**, *8*, 3766–3770.

(32) Stinson, H. T.; Sternbach, A.; Najera, O.; Jing, R.; Mcleod, A. S.; Slusar, T. V.; Mueller, A.; Anderegg, L.; Kim, H. T.; Rozenberg, M.; Basov, D. N. Imaging the nanoscale phase separation in vanadium dioxide thin films at terahertz frequencies. *Nat. Commun.* **2018**, *9*, 3604.

(33) Liewald, C.; Mastel, S.; Hesler, J.; Huber, A. J.; Hillenbrand, R.; Keilmann, F. All-electronic terahertz nanoscopy. *Optica* **2018**, *5* (2), 159-163.

(34) Giordano, M. C.; Mastel, S.; Liewald, C.; Columbo, L. L.; Brambilla, M.; Viti, L.; Politano, A.; Zhang, K.; Li, L.; Davies, A. G.; Linfield, E. H.; Hillenbrand, R.; Keilmann, F.; Scamarcio, G.; Vitiello, M. S. Phase-resolved terahertz self-detection near-field microscopy. *Opt. Express* **2018**, *26*, 18423–18435.

(35) Zhang, J.; Chen, X.; Mills, S.; Ciavatti, T.; Yao, Z.; Mescall, R.; Hu, H.; Semenenko, V.; Fei, Z.; Li, H.; Perebeinos, V.; Tao, H.; Dai, Q.; Du, X.; Liu, M. Terahertz Nanoimaging of Graphene. *ACS Photonics* **2018**, *5* (7), 2645–2651.

(36) Aghamiri, N. A.; Huth, F.; Huber, A. J.; Fali, A.; Hillenbrand, R.; Abate, Y. Hyperspectral time-domain terahertz nanoimaging. *Opt. Express* **2019**, *27* (17), 24231.

(37) Wehmeier, L.; Nörenberg, T.; de Oliveira, T. V. A. G.; Klopff, J. M.; Yang, S.; Martin, L. W.; Ramesh, R.; Eng, L. M.; Kehr, S. C. Phonon-induced near-field resonances in multiferroic BiFeO<sub>3</sub> thin films at infrared and THz wavelengths. *Appl. Phys. Lett.* **2020**, *116*, 071103.

(38) Oliveira, T. V. A. G. de; Nörenberg, T.; Álvarez-Pérez, G.; Wehmeier, L.; Taboada-Gutiérrez, J.; Obst, M.; Hempel, F.; E. Lee, J. H.; Klopff, J. M.; Errea, I.; Nikitin, A. Y.; Kehr, S. C.; Alonso-González, P.; Eng, L. M. Nanoscale-confined and low-loss terahertz phonon polaritons in a hyperbolic van der Waals crystal. arXiv:2007.06342v1.

(39) Li, P.; Yang, X. S.; Maß, T. W. W.; Hanss, J.; Lewin, J.; Michel, A. K. U.; Wuttig, M.; Taubner, T. Reversible optical switching of highly confined phonon–polaritons with an ultrathin phase-change material. *Nat. Mater.* **2016**, *15*, 870.

(40) Mooshammer, F.; Sandner, F.; Huber, M. A.; Zizlsperger, M.; Weigand, H.; Plankl, M.; Weyrich, C.; Lanius, M.; Kampmeier, J.; Mussler, G.; Grützmacher, D.; Boland, J. L.; Cocker, T. L.; Huber, R. Nanoscale Near-Field Tomography of Surface States on (Bi<sub>0.5</sub>Sb<sub>0.5</sub>)<sub>2</sub>Te<sub>3</sub>. *Nano Lett.* **2018**, *18* (12), 7515–7523.

(41) Lewin, M.; Hauer, B.; Bornhöfft, M.; Jung, L.; Benke, J.; Michel, A. K. U.; Mayer, J.; Wuttig, M.; Taubner, T. Imaging of phase change materials below a capping layer using correlative infrared nearfield microscopy and electron microscopy. *Appl. Phys. Lett.* **2015**, *107*, 151902.

(42) Kress, W.; Borik, H.; Wehner, R. K. Infrared Lattice Absorption of Silicon and Germanium. *Phys. Stat. Sol.* **1968**, *29*, 133–143.

(43) Matsunaga, T.; Yamada, N.; Kojima, R.; Shamoto, S.; Sato, M.; Tanida, H.; Uruga, T.; Kohara, S.; Takata, M.; Zalden, P.; Bruns, G.; Sergueev, L.; Wille, H. C.; Hermann, R. P.; Wuttig, M. Phase-Change Materials: Vibrational Softening upon Crystallization and Its Impact on Thermal Properties. *Adv. Funct. Mater.* **2011**, *21* (12), 2232–2239.

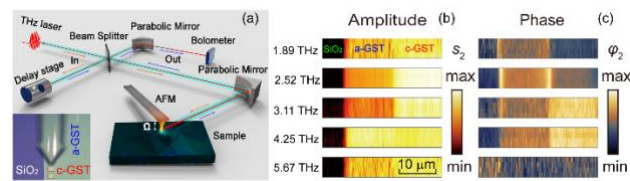
- (44) Harbecke, B. Coherent and Incoherent Reflection and Transmission of Multilayer Structures. *Appl. Phys. B* **1968**, *39*,165-170.
- (45) Chanda, G.; Lobo, R. P. S. M.; Schachinger, E.; Wosnitza, J.; Naito, M.; Pronin, A. V. Optical study of superconducting Pr<sub>2</sub>CuO<sub>x</sub> with  $x \sim 4$ . *Phys. Rev. B* **2014**, *90* (2), 024503.
- (46) Chen, C.; Jost, P.; Volker, H.; Kaminski, M.; Wirtsohn, M.; Engelmann, U.; Krüger, K.; Schlich, F.; Schlockermann, C.; Lobo, R. P. S. M.; Wuttig, M. Dielectric properties of amorphous phase-change materials. *Phys. Rev. B* **2017**, *95* (9), 094111.
- (47) Schnell, M.; Carney, P. S.; Hillenbrand, R. Synthetic optical holography for rapid nanoimaging. *Nat. Commun.* **2014**, *5*, 3499.
- (48) Mastel, S. Govyadinov, A. A.; Maissen, C.; Chuvilin, A.; Berger, A.; Hillenbrand, R. Understanding the Image Contrast of Material Boundaries in IR Nanoscopy Reaching 5 nm Spatial Resolution. *ACS Photonics* **2018**, *5* (8), 3372–3378.
- (49) Maissen, C.; Chen, S.; Nikulina, E.; Govyadinov, A.; Hillenbrand, R. Probes for Ultrasensitive THz Nanoscopy. *ACS Photonics* **2019**, *6* (5), 1279–1288.
- (50) Cvitkovic, A.; Ocelic, N.; Hillenbrand, R. Analytical model for quantitative prediction of material contrasts in scattering-type near-field optical microscopy. *Opt. Express* **2007**, *5* (14), 8550.
- (51) Hauer, B.; Engelhardt, A. P.; Taubner, T. Quasi-analytical model for scattering infrared near-field microscopy on layered systems. *Opt. Express* **2012**, *20* (12), 13173.
- (52) Mastel, S.; Lundeberg, M. B.; Alonso-González, P.; Gao, Y.; Watanabe, K.; Taniguchi, T.; Hone, J.; Koppens, F. H. L.; Nikitin, A. Y.; Hillenbrand, R. Terahertz Nanofocusing with Cantilevered Terahertz-Resonant Antenna Tips. *Nano Lett.* **2017**, *17* (11), 6526–6533.
- (53) Hillenbrand, R.; Taubner, T.; Keilmann, F. Phonon-enhanced light–matter interaction at the nanometre scale. *Nature* **2002**, *418*, 159.
- (54) Taubner, T.; Hillenbrand, R.; Keilmann, F. Performance of visible and mid-infrared scattering-type near-field optical microscopes. *J. Microsc.* **2003**, *210* (3), 311–314.
- (55) Hillenbrand, R.; Keilmann, F. Complex Optical Constants on a Subwavelength Scale. *Phys. Rev. Lett.* **2000**, *85*, 3029–3032.
- (56) Taubner, T.; Keilmann, F.; Hillenbrand, R. Effect of Tip Modulation on Image Contrast in Scattering-Type Near-Field Optical Microscopy. *J. Korean Phy. Soc.* **2005**, *47*, 213.
- (57) Walford, J. N.; Porto, J. A.; Carminati, R.; Greffet, J. J.; Adam, P. M.; Hudlet, S.; Bijeon, J. L.; Stashkevich, A.; Royer, P. Influence of tip modulation on image formation in scanning near-field optical microscopy. *J. Appl. Phys.* **2001**, *89* (9), 5159–5169.
- (58) Amarie, S.; Keilmann, F. Broadband-infrared assessment of phonon resonance in scattering-type near-field microscopy. *Phys. Rev. B* **2011**, *84*, 199904.
- (59) Aizpurua, J.; Taubner, T.; Abajo, F. J. G. de; Brehm, M.; Hillenbrand, R. Substrate-enhanced infrared near-field spectroscopy, *Opt. Express* **2008**, *16* (3), 1529.
- (60) Krutokhvostov, R.; Govyadinov, A. A.; Stiegler, J. M.; Huth, F.; Chuvilin, A.; Carney, P. S.; Hillenbrand, R. Enhanced resolution in subsurface near-field optical microscopy, *Opt. Express* **2012**, *20* (1), 593.

- (61) Eisele, M.; Cocker, T. L.; Huber, M. A.; Plankl, M.; Viti, L.; Ercolani, D.; Sorba, L.; Vitiello, M. S.; Huber, R. Ultrafast multi-terahertz nano-spectroscopy with sub-cycle temporal resolution, *Nat. Photonics* **2014**, 8 (11), 841.
- (62) Yao, Z.; Semenenko, V.; Zhang, J.; Mills, S.; Zhao, X.; Chen, X.; Hu, H.; Mescall, R.; Ciavatti, T.; March, S.; Bank, S. R.; Tao, T. H.; Zhang, X.; Perebeinos, V.; Dai, Q.; Du, X.; Liu, M. Photo-induced terahertz near-field dynamics of graphene/InAs heterostructures, *Opt. Express* **2019**, 27 (10), 13611.

For Table of Contents use only

## Terahertz nanoimaging and nanospectroscopy of chalcogenide phase-change materials

Chao Chen<sup>1†</sup>, Shu Chen<sup>2†</sup>, Ricardo P.S.M. Lobo<sup>3,4</sup>, Carlos Maciel-Escudero<sup>2,5</sup>, Martin Lewin<sup>6</sup>, Thomas Taubner<sup>6</sup>, Wei Xiong<sup>1</sup>, Ming Xu<sup>1\*</sup>, Xinliang Zhang<sup>1</sup>, Xiangshui Miao<sup>1</sup>, Peining Li<sup>1\*</sup>, Rainer Hillenbrand<sup>7,8\*</sup>



We demonstrate that the optical phonons of amorphous and crystalline phases of chalcogenide phase-change materials (PCMs) can be studied by frequency-tunable THz scattering-type scanning near-field optical microscopy (s-SNOM).